JOC The Journal of Organic Chemistry

pubs.acs.org/joc Note

Phospha-RosIndolizine Dye with Shortwave Infrared (SWIR) Absorption and Emission

Matthew A. Saucier,* Nicholas A. Kruse, Brennan E. Seidel, Nathan I. Hammer, Gregory S. Tschumper, and Jared H. Delcamp

Cite This: J. Org. Chem. 2024, 89, 9092−9097 Read Online

ACCESS | Metrics & More | Article Recommendations | Supporting Information

ABSTRACT: Shortwave infrared (SWIR, 1000−1700 nm) absorbing and emitting dyes are needed for infrared diodes and sensors used in a wide variety of industrial and medical applications. Herein, an electron-withdrawing phosphine oxide (P═O) substituted xanthene is coupled with strong indolizine donors to produce a SWIR absorbing (λ_{abs} = 1294 nm in DCM) and emitting (λ_{emis} = 1450 nm in DCM) dye called **PRos1450**. The unique properties of this dye are characterized via photophysical, electrochemical, and computational analyses.

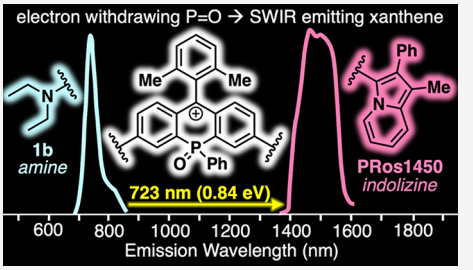

Chromophores that exhibit electronic transitions in the shortwave infrared (SWIR, 1000−1700 nm) region are in great need for the development of infrared diodes, photoconductor sensors, and fluorescent probes used in a wide variety of applications such as species tracking, topological mapping, and *in vivo* biological imaging.[1−8] The most common materials in use for SWIR photodetectors remain inorganic metal composites like InGaAs, InAs, HgCdTe, and quantum dots despite their raw material cost and need for cooling to eliminate dark current.[9−17] Organic polymers offer lower cost solution processability and ambient operating temperatures, but find accessing longer wavelength photocurrent response to remain a challenge.[18−21] SWIR emitting organic dyes are also needed for use in fluorescence biological imaging since longer emission wavelengths lead to improved imaging quality.[22−25] However, very few small-molecule probes have been reported with fluorescence wavelengths longer than 1400 nm.[26−28] Thus, developing new organic small molecules that possess these SWIR properties is necessary.

Rhodamine and xanthene dyes have been extensively studied for over a century.[29−31] These dyes absorb and emit strongly, having extensive use in biological imaging and cellular microscopy.[32−35] Furthermore, the photophysical parameters—namely, the peak emission wavelength (λ_{emis})—of these dyes are extremely tunable with both donor and core modifications.[32,36−40] Replacing the functional group in the central ring of the xanthene core with electron-donating (e.g., O, N), -neutral (e.g., C, Si), and -withdrawing (e.g., SO_2, C═O, P═O)[37,38,41−44] groups can dramatically shift λ_{emis} to shorter or longer wavelengths. The phosphine oxide (P═O) substituted xanthenes, like **1b**,[42] display some of the longest λ_{emis} that can be accessed through core modifications alone, and this moiety has also been shown to improve dye stability.[37,38,40,45,46] Core modifications which delete the central atom altogether have also been used to shift peak absorption wavelength (λ_{abs}) to longer wavelengths; however, these dyes exhibit much less intense absorption (∼1/3rd the molar absorptivity) and emission (low or undetectable).[47,48] Our group has previously demonstrated how replacing traditional amine donors with indolizine donors produces a substantial shift of λ_{emis} toward longer wavelengths in O- and Si-substituted xanthenes (**^{tol}RosIndz**[49] and **SiRos1300**,[28,50] Figure 1). With this in mind, we hypothesize that replacing the amine donors in a xanthene substituted with an electron-withdrawing P═O group in the central ring (**1b**) with stronger fully conjugated indolizine donors (**PRos1450**) would pave a direct path toward longer wavelength SWIR emitting small-molecule chromophores (Figure 1).

To synthesize **PRos1450** (Scheme 1), **1** was prepared according to literature precedent.[52] Then, **1** underwent a double lithium−halogen exchange reaction with *n*-butyllithium (BuLi) followed by addition of *P*,*P*-dichlorophenylphosphine ($PhPCl_2$) and hydrogen peroxide (H_2O_2) to form a triarylphosphine oxide intermediate, which was oxidized with sodium hydroxide (NaOH), tetrabutylammonium bromide (TBAB), and oxygen from the air to form the phospha-xanthone core (**2**) in 22% yield over 3 steps. Then, to append indolizine donors to **2**, 1-methyl-2-phenyl indolizine (**3**, synthesized according to literature precedent[53]) was used in a palladium-catalyzed C−H activation reaction using con-

Received: March 25, 2024
Revised: May 14, 2024
Accepted: May 17, 2024
Published: June 6, 2024

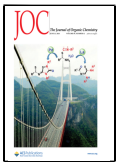

https://doi.org/10.1021/acs.joc.4c00741
J. Org. Chem. 2024, 89, 9092−9097

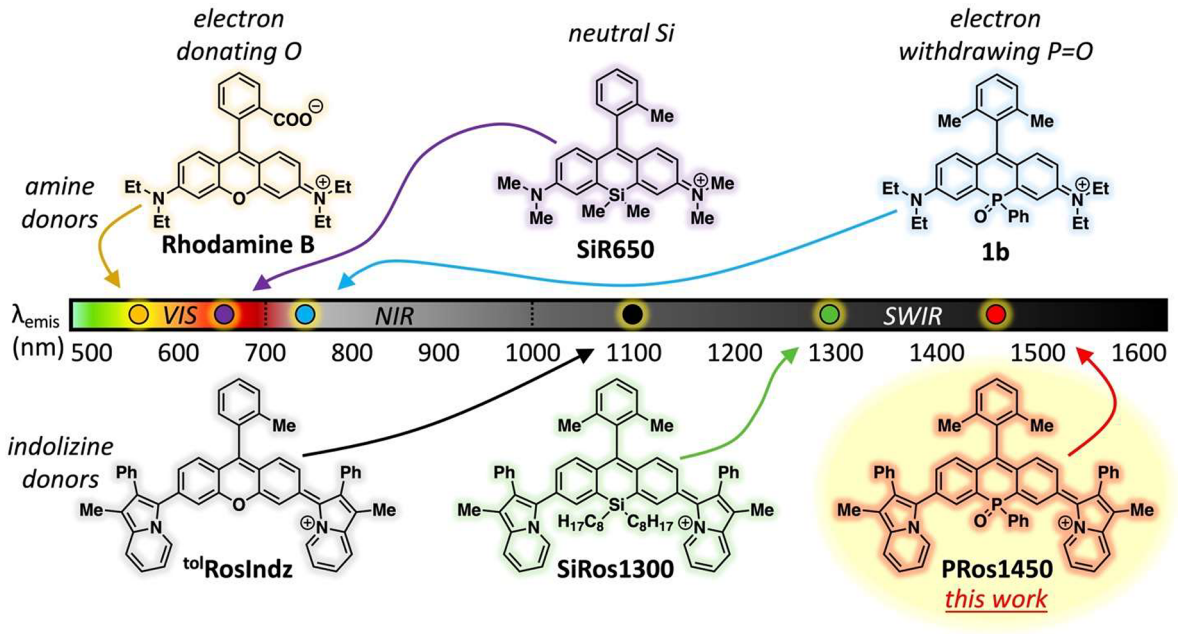

Figure 1. Emission wavelength of xanthene series with electron-donating O (left), neutral Si (middle), or electron-withdrawing P═O (right) substituted cores with amine (top) and indolizine (bottom) donors.[28,33,42,49,51]

Scheme 1. Synthetic Design of Indolizine Phospha-Rosindolizine Dye PRos1450

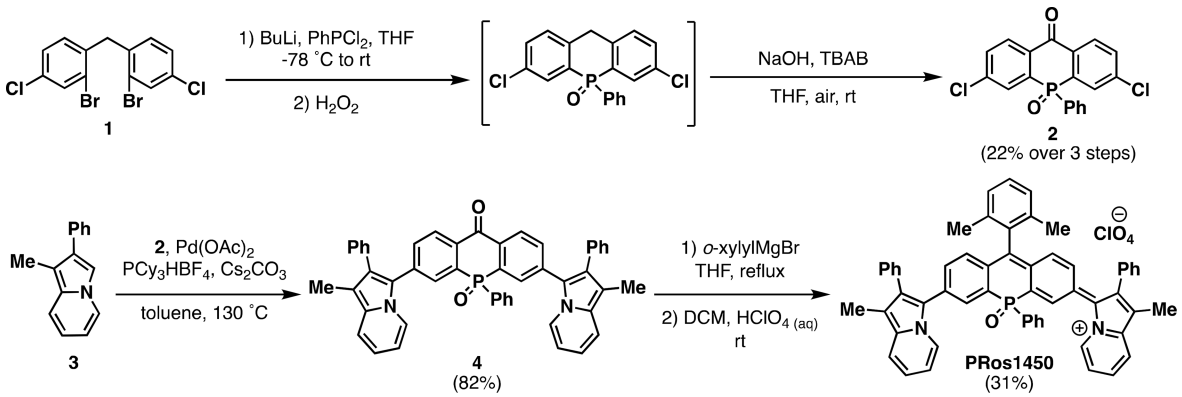

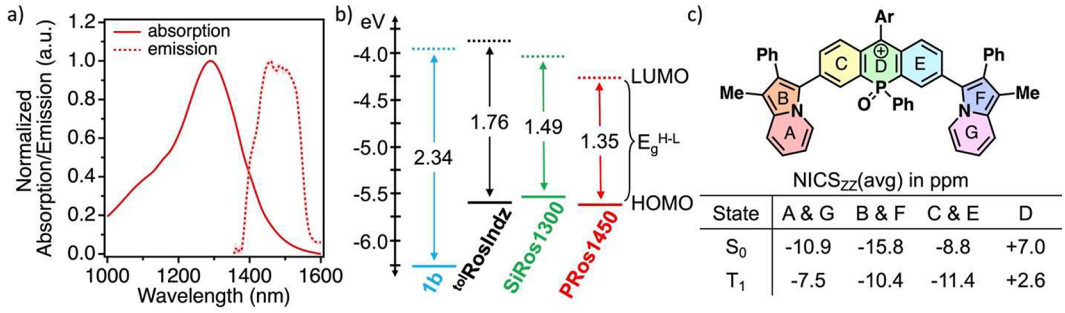

Figure 2. (a) Absorption (solid) and emission (dashed) spectra of **PRos1450** in DCM. The emission signal is near the limit of the detector used, and curve shape may differ with a detector extending further in the SWIR. (b) Frontier molecular orbital energies (solid = HOMO, dashed = LUMO) and HOMO−LUMO energy gap ($E_g^{H\text{-}L}$) of **1b**, **tolRosIndz**, **SiRos1300**,[47] and **PRos1450**. (c) Ring naming system and $NICS_{ZZ}$(avg) values (average of $NICS_{ZZ}(+1)$ and $NICS_{ZZ}(-1)$) in ppm for **PRos1450** (Ar = *o*-xylyl).

ditions previously optimized for indolizine arylation[28,49] to afford the ketone (**4**) in 82% yield. The 2-phenyl and 1-methyl substituents on the indolizine leave the primary coupling site at the 3-position. No other isomers in the coupling reaction were observed or isolated, and previous crystallography studies suggest similar connectivity to that described herein.[47,54] Grignard addition of commercial *ortho*-xylyl magnesium bromide followed by stirring with aqueous perchloric acid ($HClO_4$) gave the final cationic dye in 31% yield.

The photophysical properties of **PRos1450** were studied in 12 different organic solvents (Figures S1 and S2). The dye behaves most cyanine-like with a $\pi-\pi^*$ transition (where the

https://doi.org/10.1021/acs.joc.4c00741
J. Org. Chem. 2024, 89, 9092−9097

Table 1. Photophysical and Electrochemical Data for PRos1450 in a DCM Solution[a]

dye	λ_{abs} (nm)	λ_{onset} (nm)	λ_{emis} (nm)	ε (M^{-1} cm^{-1})	$E_{S+/S}$ (V)	$E_{S/S-}$ (V)	$E_{S+/S*}$ (V)	E_g^{opt} (eV)
PRos1450	1294	1474	1450	61,000	−0.25	−1.18	−1.08	0.84
SiRos1300[b]	1140	1350	1300	115,000	−0.45	−1.68	−1.37	0.92
^{tol}RosIndz[c]	930	1042	1097	79,500	−0.65	−1.70	−1.84	1.19
1b[d]	708		734	99,300				

[a]Electrochemical potentials shown are referenced to Fc^+/Fc at 0.00 V in DCM with a 0.1 M Bu_4NPF_6 supporting electrolyte under an Ar atmosphere. [b]Previously reported in DCM solution.[28] [c]Photophysical data previously reported in toluene;[49] electrochemical data previously reported in DCM.[47] [d]Photophysical data previously reported in PBS solution; electrochemical data and onset wavelength not provided.[42]

lowest energy transition is sharp and intense) between 1200 and 1300 nm in nonpolar halogenated solvents like dichloromethane (DCM), dichloroethane (DCE), and chloroform ($CHCl_3$). In all the other solvents studied, the dye displays a broad absorption from 900 to 1400 nm, probably arising from stabilization of localized charges in the cationic dye, leading to increased charge transfer behavior in solution. Furthermore, peaks at 540 and 870 nm arise in the absorption spectrum taken in solvents such as acetonitrile (MeCN), methanol (MeOH), ethyl acetate (EtOAc), and acetone, which align with peaks observed in a concentrated DCE spectrum, which may suggest that those absorption features are aggregation induced (Figure S3). **PRos1450** absorbs and emits at longer wavelengths (λ_{abs} = 1294 nm and λ_{emis} = 1450 nm in DCM, Figure 2a) than previous dyes **1b**, **^{tol}RosIndz**, and **SiRos1300**. Notably, the switch from amine donors to indolizines produces a shift to longer wavelengths of λ_{abs} and λ_{emis} by 0.79 eV (586 nm) and 0.84 eV (723 nm), respectively (Table 1). The trend in molar absorptivity (ε) agrees with previously work[38] where from highest to lowest ε the trend is neutral substituted xanthenes (Si, **SiRos1300** = 115,000 M^{-1} cm^{-1}) > electron-donating substituted xanthenes (O, **^{tol}RosIndz** = 79,500 M^{-1} cm^{-1}) > electron-withdrawing substituted xanthenes (P═O, **PRos1450** = 61,000 M^{-1} cm^{-1}). The fundamental reason for this trend in ε across xanthene dyes is not well explored but presumably comes from increased overlap of the frontier molecular orbitals partaking in the electronic transition for neutral substituents compared to donating or withdrawing substituents. In photostability experiments (Figure S5), **PRos1450** shows a negligible decrease in absorption intensity over 24 h (93%) under constant ambient indoor lighting and maintains a significant absorbance at 1294 nm for 2−3 days (63−30%). Although an emission spectrum was obtained for **PRos1450**, a fluorescence quantum yield was not calculated because the emission peak was near the end of the detectivity limit of the InGaAs detector used.

In cyclic voltammetry (CV) measurements of **PRos1450** in DCM referencing ferrocenium/ferrocene at 0.00 V (Figure S4), the ground state oxidation potential ($E_{S+/S}$) is shifted to more positive potentials (−0.25 V) compared to **^{tol}RosIndz** (−0.65 V) and **SiRos1300** (−0.45 V). The same trend is also found in the ground state reduction potential ($E_{S/S-}$), where the energy level is shifted to more positive potentials (−1.18 V) compared to **^{tol}RosIndz** (−1.70 V) and **SiRos1300** (−1.68 V). These observations are consistent with the addition of a stronger withdrawing group to the xanthene core that lowers the frontier molecular orbital energies. Using the onset absorption wavelength (λ_{onset}, determined using the 0nset program[55]) the optical energy gap (E_g^{opt}) can be determined using the equation $E_g^{opt} = 1240/\lambda_{onset}$. As λ_{abs} increases across the series, E_g^{opt} shrinks (**^{tol}RosIndz** = 1.19 eV, **SiRos1300** = 0.92 eV, **PRos1450** = 0.84 eV). Thus, while both frontier molecular orbitals are being stabilized by the addition of a withdrawing group to the xanthene core, the amount of stabilization is more for one of the orbitals, presumably the lowest unoccupied molecular orbital (LUMO).

Similar to previous studies of comparable NIR and SWIR dyes,[28,49,56,57] all computational calculations were conducted at the B3LYP/6-311G(d,p)[58−60] level of theory using a DCM polarizable continuum model[61−64] as implicit solvent with Gaussian16[65] software. Density functional theory (DFT) calculations (Table S1 and Figure 2b) show that the highest occupied molecular orbital (HOMO) is raised significantly (643 mV) switching from an amine donor (**1b**) to an indolizine donor (**PRos1450**), which helps to shrink the HOMO−LUMO energy gap (E_g^{H-L}). The HOMO energy level stays nearly the same across the series of indolizine xanthene dyes (**^{tol}RosIndz**, **SiRos1300**, and **PRos1450**, within 80 mV), which corresponds to the identical indolizine donor used. However, the LUMO drops significantly from **^{tol}RosIndz** > **SiRos1300** > **PRos1450** (428 mV difference between **^{tol}RosIndz** and **PRos1450**) due to the changing substituent in the xanthene core, which—consistent with previous work[38]—contributes to the shrinking E_g^{H-L}. Visualization of the HOMO and LUMO orbitals in **PRos1450** (Figure S7) shows delocalization across the entire π-system. Time-dependent DFT (TD-DFT) calculations were also performed (Table S1) to correlate with the solution phase photophysical data. Vertical transition (VT) energies decrease across the series **1b** > **^{tol}RosIndz** > **SiRos1300** > **PRos1450**. The differences in VT energies between **PRos1450** and **1b** (0.91 eV), **^{tol}RosIndz** (0.24 eV), and **SiRos1300** (0.08 eV) are similar to the differences in maximum λ_{abs} (0.79, 0.38, and 0.13 eV, respectively). These data demonstrate how modifying both the functional group in the center of the xanthene core (O vs Si vs P═O) and the appended donors (amine vs indolizine) can change the molecular orbital configuration and result in modulation of λ_{abs}. Interestingly, another property that arises from decreasing E_g^{H-L} and λ_{abs} energies is an increase in thermally accessible diradical states. **PRos1450** displays the lowest energy singlet−triplet energy gap (ΔE_{ST}) of the series of dyes compared herein (12.2 kcal/mol). Between this relatively low computed ΔE_{ST} and the lack of sharp and defined peaks in the ^{1}H NMR spectrum, **PRos1450** may have some thermal population of a diradical triplet state.

Nucleus-independent chemical shift (NICS)[66−70] calculations were performed (Figure 2c and Table S3) using the optimized singlet ground state (S_0) and the first triplet state (T_1) of **PRos1450**. $NICS_{ZZ}$(avg) values reported in Figure 2c are the average of the $NICS_{ZZ}(+1)$ and $NICS_{ZZ}(-1)$ values (at 1 Å above and below each ring). Consistent with previous reports,[57,71] the T_1 state is used as an approximation of the excited state since the magnetic shielding tensors are not available via TD-DFT for the S_1 state with our computational

https://doi.org/10.1021/acs.joc.4c00741
J. Org. Chem. 2024, 89, 9092−9097

software. The indolizine rings are aromatic in the ground state (A and G = −10.9 ppm, B and F = −15.8 ppm) and remain aromatic in the excited state but slightly less so (A and G = −7.5 ppm, B and F = −10.4 ppm). The central ring containing the phosphorus atom is antiaromatic in the ground state (D = +7.0 ppm) and, interestingly, becomes more aromatic in the excited state (D = +2.6 ppm). The adjacent benzene rings are aromatic in the ground state (C and E = −8.8 ppm) and—similar to ring D—become more aromatic in the excited state (C and E = −11.4 ppm). This shift in ring D from antiaromatic in the ground state to more aromatic in the excited state follows closely with Baird's rule,[72] since the central ring can be drawn as a homoaromatic 4n π-electron cationic system consistent with weak antiaromaticity (Figure 2c). Also, this trend is seen when comparing **PRos1450** to our previous NICS calculations[47] on ^{tol}**RosIndz** and **SiRos1300**, where ^{tol}**RosIndz** changes from being aromatic in the ground state (−4.8 ppm) to antiaromatic in the excited state (+11.0 ppm) and **SiRos1300** remains antiaromatic in both the ground state (+9.1 ppm) and the excited state (+7.5 ppm).

A unique phospha-rosindolizine dye (**PRos1450**) was synthesized herein and displayed a significantly shifted λ_{emis} (723 nm or 0.84 eV shift) to lower energy compared to that of the previous amine donor phospha-rosamine analogue (**1b**). The photophysical properties of the dye were described with absorption spectroscopy in 12 different organic solvents, showing the most cyanine-like absorption features in DCM, DCE, and $CHCl_3$. Electrochemical potentials were obtained in DCM solution and show a decreasing optical energy gap (E_g^{opt}) across the series of indolizine-appended xanthenes (^{tol}**RosIndz** > **SiRos1300** > **PRos1450**). DFT and TD-DFT computations corroborate the photophysical and electrochemical data where both the vertical transition energy and HOMO−LUMO band gap decrease as ^{tol}**RosIndz** > **SiRos1300** > **PRos1450**. **PRos1450** is an exceptionally long wavelength absorbing and emitting dye, especially compared to other indolizine-based dyes (Figure S6), which provides an example dye design from which to work for future iterations.

■ ASSOCIATED CONTENT

Data Availability Statement

The data underlying this study are available in the published article and its Supporting Information.

Supporting Information

The Supporting Information is available free of charge at https://pubs.acs.org/doi/10.1021/acs.joc.4c00741.

Experimental details, synthetic procedures and characterization data, NMR and HRMS spectra of new compounds, additional absorption spectra, electrochemical spectra and data (including cyclic voltammetry), photostability plots, a comparison to previous dyes with indolizine donors, DFT and TD-DFT computational data, NICS data and profiles, and coordinates for optimized geometries obtained in DFT computations (PDF)

■ AUTHOR INFORMATION

Corresponding Author

Matthew A. Saucier − *Department of Chemistry and Biochemistry, University of Mississippi, University, Mississippi 38677, United States;* orcid.org/0000-0002-2565-0806; Email: masaucie@go.olemiss.edu

Authors

Nicholas A. Kruse − *Department of Chemistry and Biochemistry, University of Mississippi, University, Mississippi 38677, United States*

Brennan E. Seidel − *Department of Chemistry and Biochemistry, University of Mississippi, University, Mississippi 38677, United States*

Nathan I. Hammer − *Department of Chemistry and Biochemistry, University of Mississippi, University, Mississippi 38677, United States;* orcid.org/0000-0002-6221-2709

Gregory S. Tschumper − *Department of Chemistry and Biochemistry, University of Mississippi, University, Mississippi 38677, United States;* orcid.org/0000-0002-3933-2200

Jared H. Delcamp − *Department of Chemistry and Biochemistry, University of Mississippi, University, Mississippi 38677, United States;* orcid.org/0000-0001-5313-4078

Complete contact information is available at: https://pubs.acs.org/10.1021/acs.joc.4c00741

Notes

The authors declare no competing financial interest.

■ ACKNOWLEDGMENTS

We acknowledge and thank the University of Mississippi School of Pharmacy GlyCORE mass spectrometry facility. Mass spectrometry research reported in this publication was supported by an Institutional Development Award (IDeA) from the National Institute of General Medical Sciences of the National Institute of Health under award number P20GM130460. This work was funded by the National Science Foundation grant numbers OIA-1757220 and CHE-2154403. All authors have read and agreed to the manuscript.

■ REFERENCES

(1) De Silva, V.; Roche, J.; Kondoz, A. Robust Fusion of LiDAR and Wide-Angle Camera Data for Autonomous Mobile Robots. *Sensors* **2018**, *18* (8), 2730.

(2) Meylan, M. C. Short Wavelength Infrared Lidar. WO2019223858A1, November 28, 2019. https://patents.google.com/patent/WO2019223858A1/en (accessed 2024−02−07).

(3) Huerta, M. *SWIR Use In Autonomous Cars*. SeeDevice. https://seedevice.com/blog/swir-use-in-autonomous-cars (accessed 2024−02−07).

(4) Hadji, B. *Understanding wavelength choice in LiDAR systems*. Embedded.com. https://www.embedded.com/understanding-wavelength-choice-in-lidar-systems/ (accessed 2024−02−07).

(5) Debnath, S.; Paul, M.; Debnath, T. Applications of LiDAR in Agriculture and Future Research Directions. *Journal of Imaging* **2023**, *9* (3), 57.

(6) Brydegaard, M. Advantages of Shortwave Infrared LIDAR Entomology. *Imaging and Applied Optics 2014*; Optica Publishing Group, 2014; OSA Technical Digest, LW2D.6.

(7) Li, H.; Wang, X.; Li, X.; Zeng, S.; Chen, G. Clearable Shortwave-Infrared-Emitting NaErF4 Nanoparticles for Noninvasive Dynamic Vascular Imaging. *Chem. Mater.* **2020**, *32* (8), 3365−3375.

(8) Chinnathambi, S.; Shirahata, N. Recent Advances on Fluorescent Biomarkers of Near-Infrared Quantum Dots for in Vitro and in Vivo Imaging. *Sci. Technol. Adv. Mater.* **2019**, *20* (1), 337−355.

(9) Sun, X.; Abshire, J. B.; Beck, J. D.; Mitra, P.; Reiff, K.; Yang, G. HgCdTe Avalanche Photodiode Detectors for Airborne and Spaceborne Lidar at Infrared Wavelengths. *Opt. Express, OE* **2017**, *25* (14), 16589−16602.

(10) Wolley, O.; Mekhail, S.; Moreau, P.-A.; Gregory, T.; Gibson, G.; Leuchs, G.; Padgett, M. J. Near Single-Photon Imaging in the

Shortwave Infrared Using Homodyne Detection. *Proc. Natl. Acad. Sci. U. S. A.* **2023**, *120* (10), No. e2216678120.
(11) Chen, B.; Chen, Y.; Deng, Z. Recent Advances in High Speed Photodetectors for eSWIR/MWIR/LWIR Applications. *Photonics* **2021**, *8* (1), 14.
(12) Vittadello, L.; Klenen, J.; Koempe, K.; Kocsor, L.; Szaller, Z.; Imlau, M. NIR-to-NIR Imaging: Extended Excitation Up to 2.2 Mm Using Harmonic Nanoparticles with a Tunable hIGh EneRgy (TIGER) Widefield Microscope. *Nanomaterials* **2021**, *11* (12), 3193.
(13) Sordillo, D. C.; Sordillo, L. A.; Sordillo, P. P.; Shi, L.; Alfano, R. R. Short Wavelength Infrared Optical Windows for Evaluation of Benign and Malignant Tissues. *J. Biomed. Opt* **2017**, *22* (4), 045002.
(14) Wen, H.; Bellotti, E. Numerical Study of the Intrinsic Recombination Carriers Lifetime in Extended Short-Wavelength Infrared Detector Materials: A Comparison between InGaAs and HgCdTe. *J. Appl. Phys.* **2016**, *119* (20), 205702.
(15) Pejovic, V.; Georgitzikis, E.; Lee, J.; Lieberman, I.; Cheyns, D.; Heremans, P.; Malinowski, P. E. Infrared Colloidal Quantum Dot Image Sensors. *IEEE Trans. Electron Devices* **2022**, *69* (6), 2840−2850.
(16) Attiaoui, A.; Bouthillier, E.; Daligou, G.; Kumar, A.; Assali, S.; Moutanabbir, O. Extended Short-Wave Infrared Absorption in Group-IV Nanowire Arrays. *Phys. Rev. Appl.* **2021**, *15* (1), 014034.
(17) Yang, Y.; Zhang, Y. H.; Shen, W. Z.; Liu, H. C. Semiconductor Infrared Up-Conversion Devices. *Prog. Quantum Electron.* **2011**, *35* (4), 77−108.
(18) Wu, Z.; Zhai, Y.; Kim, H.; Azoulay, J. D.; Ng, T. N. Emerging Design and Characterization Guidelines for Polymer-Based Infrared Photodetectors. *Acc. Chem. Res.* **2018**, *51* (12), 3144−3153.
(19) Li, N.; Lan, Z.; Lau, Y. S.; Xie, J.; Zhao, D.; Zhu, F. SWIR Photodetection and Visualization Realized by Incorporating an Organic SWIR Sensitive Bulk Heterojunction. *Adv. Sci.* **2020**, *7* (14), 2000444.
(20) Li, N.; Park, I.; Vella, J. H.; Oh, S. J.; Azoulay, J. D.; Leem, D.-S.; Ng, T. N. Contribution of Sub-Gap States to Broadband Infrared Response in Organic Bulk Heterojunctions. *ACS Appl. Mater. Interfaces* **2022**, *14* (47), 53111−53119.
(21) Li, N.; Mahalingavelar, P.; Vella, J. H.; Leem, D.-S.; Azoulay, J. D.; Ng, T. N. Solution-Processable Infrared Photodetectors: Materials, Device Physics, and Applications. *Materials Science and Engineering: R: Reports* **2021**, *146*, 100643.
(22) Hong, G.; Antaris, A. L.; Dai, H. Near-Infrared Fluorophores for Biomedical Imaging. *Nat. Biomed. Eng.* **2017**, *1* (1), 1−22.
(23) Carr, J. A.; Aellen, M.; Franke, D.; So, P. T. C.; Bruns, O. T.; Bawendi, M. G. Absorption by Water Increases Fluorescence Image Contrast of Biological Tissue in the Shortwave Infrared. *Proc. Natl. Acad. Sci. U. S. A.* **2018**, *115* (37), 9080−9085.
(24) Sun, C.; Li, B.; Zhao, M.; Wang, S.; Lei, Z.; Lu, L.; Zhang, H.; Feng, L.; Dou, C.; Yin, D.; Xu, H.; Cheng, Y.; Zhang, F. J-Aggregates of Cyanine Dye for NIR-II in Vivo Dynamic Vascular Imaging beyond 1500 Nm. *J. Am. Chem. Soc.* **2019**, *141* (49), 19221−19225.
(25) Wang, Z.; Wang, X.; Wan, J.-B.; Xu, F.; Zhao, N.; Chen, M. Optical Imaging in the Second Near Infrared Window for Vascular Bioimaging. *Small* **2021**, *17* (43), 2103780.
(26) Liu, M.-H.; Zhang, Z.; Yang, Y.-C.; Chan, Y.-H. Polymethine-Based Semiconducting Polymer Dots with Narrow-Band Emission and Absorption/Emission Maxima at NIR-II for Bioimaging. *Angew. Chem., Int. Ed.* **2021**, *60* (2), 983−989.
(27) Yang, Y.; Sun, C.; Wang, S.; Yan, K.; Zhao, M.; Wu, B.; Zhang, F. Counterion-Paired Bright Heptamethine Fluorophores with NIR-II Excitation and Emission Enable Multiplexed Biomedical Imaging. *Angew. Chem., Int. Ed.* **2022**, *61* (24), No. e202117436.
(28) Meador, W. E.; Lin, E. Y.; Lim, I.; Friedman, H. C.; Ndaleh, D.; Shaik, A. K.; Hammer, N. I.; Yang, B.; Caram, J. R.; Sletten, E. M.; Delcamp, J. H. Silicon-RosIndolizine Fluorophores with Shortwave Infrared Absorption and Emission Profiles Enable in Vivo Fluorescence Imaging. *Nat. Chem.* **2024**, 1−9.
(29) *Fluorescein*. American Chemical Society. https://www.acs.org/molecule-of-the-week/archive/f/fluorescein.html (accessed 2023−11−15).
(30) Lavis, L. D. Teaching Old Dyes New Tricks: Biological Probes Built from Fluoresceins and Rhodamines. *Annu. Rev. Biochem.* **2017**, *86*, 825−843.
(31) Bar, N.; Chowdhury, P. A Brief Review on Advances in Rhodamine B Based Chromic Materials and Their Prospects. *ACS Appl. Electron. Mater.* **2022**, *4* (8), 3749−3771.
(32) Bucevičius, J.; Gerasimaitė, R.; Kiszka, K. A.; Pradhan, S.; Kostiuk, G.; Koenen, T.; Lukinavičius, G. A General Highly Efficient Synthesis of Biocompatible Rhodamine Dyes and Probes for Live-Cell Multicolor Nanoscopy. *Nat. Commun.* **2023**, *14* (1), 1306.
(33) Kushida, Y.; Nagano, T.; Hanaoka, K. Silicon-Substituted Xanthene Dyes and Their Applications in Bioimaging. *Analyst* **2015**, *140* (3), 685−695.
(34) Rajasekar, M. Recent Trends in Rhodamine Derivatives as Fluorescent Probes for Biomaterial Applications. *J. Mol. Struct.* **2021**, *1235*, 130232.
(35) East, A. K.; Lee, M. C.; Smaga, L. P.; Jiang, C.; Mallojjala, S. C.; Hirschi, J. S.; Chan, J. Synthesis of Silicon-Substituted Hemicyanines for Multimodal SWIR Imaging. *Org. Lett.* **2022**, *24* (46), 8509−8513.
(36) Wang, L.; Du, W.; Hu, Z.; Uvdal, K.; Li, L.; Huang, W. Hybrid Rhodamine Fluorophores in the Visible/NIR Region for Biological Imaging. *Angew. Chem., Int. Ed.* **2019**, *58* (40), 14026−14043.
(37) Lv, X.; Gao, C.; Han, T.; Shi, H.; Guo, W. Improving the Quantum Yields of Fluorophores by Inhibiting Twisted Intramolecular Charge Transfer Using Electron-Withdrawing Group-Functionalized Piperidine Auxochromes. *Chem. Commun.* **2020**, *56* (5), 715−718.
(38) Daly, H. C.; Matikonda, S. S.; Steffens, H. C.; Ruehle, B.; Resch-Genger, U.; Ivanic, J.; Schnermann, M. J. Ketone Incorporation Extends the Emission Properties of the Xanthene Scaffold Beyond 1000 Nm. *Photochem. Photobiol.* **2022**, *98* (2), 325−333.
(39) Beija, M.; Afonso, C. A. M.; Martinho, J. M. G. Synthesis and Applications of Rhodamine Derivatives as Fluorescent Probes. *Chem. Soc. Rev.* **2009**, *38* (8), 2410−2433.
(40) Deng, F.; Xu, Z. Heteroatom-Substituted Rhodamine Dyes: Structure and Spectroscopic Properties. *Chin. Chem. Lett.* **2019**, *30* (10), 1667−1681.
(41) Takahashi, S.; Kagami, Y.; Hanaoka, K.; Terai, T.; Komatsu, T.; Ueno, T.; Uchiyama, M.; Koyama-Honda, I.; Mizushima, N.; Taguchi, T.; Arai, H.; Nagano, T.; Urano, Y. Development of a Series of Practical Fluorescent Chemical Tools To Measure pH Values in Living Samples. *J. Am. Chem. Soc.* **2018**, *140* (18), 5925−5933.
(42) Grzybowski, M.; Taki, M.; Senda, K.; Sato, Y.; Ariyoshi, T.; Okada, Y.; Kawakami, R.; Imamura, T.; Yamaguchi, S. A Highly Photostable Near-Infrared Labeling Agent Based on a Phospha-Rhodamine for Long-Term and Deep Imaging. *Angew. Chem., Int. Ed.* **2018**, *57* (32), 10137−10141.
(43) Chai, X.; Cui, X.; Wang, B.; Yang, F.; Cai, Y.; Wu, Q.; Wang, T. Near-Infrared Phosphorus-Substituted Rhodamine with Emission Wavelength above 700 Nm for Bioimaging. *Chem. - Eur. J.* **2015**, *21* (47), 16754−16758.
(44) Liu, J.; Sun, Y.-Q.; Zhang, H.; Shi, H.; Shi, Y.; Guo, W. Sulfone-Rhodamines: A New Class of Near-Infrared Fluorescent Dyes for Bioimaging. *ACS Appl. Mater. Interfaces* **2016**, *8* (35), 22953−22962.
(45) Fukazawa, A.; Suda, S.; Taki, M.; Yamaguchi, E.; Grzybowski, M.; Sato, Y.; Higashiyama, T.; Yamaguchi, S. Phospha-Fluorescein: A Red-Emissive Fluorescein Analogue with High Photobleaching Resistance. *Chem. Commun.* **2016**, *52* (6), 1120−1123.
(46) Zhou, X.; Lai, R.; Beck, J. R.; Li, H.; Stains, C. I. Nebraska Red: A Phosphinate-Based near-Infrared Fluorophore Scaffold for Chemical Biology Applications. *Chem. Commun.* **2016**, *52* (83), 12290−12293.
(47) Meador, W. E.; Saucier, M. A.; Tucker, M. R.; Mobley, A. J.; Parkin, S. R.; Clark, K. M.; Tschumper, G. S.; Delcamp, J. H. Extended Shortwave Infrared Absorbing Antiaromatic Fluorenium-Indolizine Chromophores. *Chem. Sci.*, **2024**

https://doi.org/10.1021/acs.joc.4c00741
J. Org. Chem. 2024, 89, 9092−9097

(48) Grzybowski, M.; Morawski, O.; Nowak, K.; Garbacz, P. Fluorene Analogues of Xanthenes - Low Molecular Weight near-Infrared Dyes. *Chem. Commun.* **2022**, *58* (36), 5455−5458.
(49) Chatterjee, S.; Meador, W. E.; Smith, C.; Chandrasiri, I.; Zia, M. F.; Nguyen, J.; Dorris, A.; Flynt, A.; Watkins, D. L.; Hammer, N. I.; Delcamp, J. H. SWIR Emissive RosIndolizine Dyes with Nanoencapsulation in Water Soluble Dendrimers. *RSC Adv.* **2021**, *11* (45), 27832−27836.
(50) Meador, W. E.; Lewis, T. A.; Shaik, A. K.; Wijesinghe, K. H.; Yang, B.; Dass, A.; Hammer, N. I.; Delcamp, J. H. Molecular Engineering of Stabilized Silicon-Rosindolizine Shortwave Infrared Fluorophores. *J. Org. Chem.* **2024**, *89* (5), 2825−2839.
(51) Scott, P.; Steve, J. *Rhodamine B*. OMLC. https://omlc.org/spectra/PhotochemCAD/html/009.html (accessed 2024−02−05).
(52) Ando, N.; Soutome, H.; Yamaguchi, S. Near-Infrared Fluorescein Dyes Containing a Tricoordinate Boron Atom. *Chem. Sci.* **2019**, *10* (33), 7816−7821.
(53) Huckaba, A. J.; Giordano, F.; McNamara, L. E.; Dreux, K. M.; Hammer, N. I.; Tschumper, G. S.; Zakeeruddin, S. M.; Grätzel, M.; Nazeeruddin, M. K.; Delcamp, J. H. Indolizine-Based Donors as Organic Sensitizer Components for Dye-Sensitized Solar Cells. *Adv. Energy Mater.* **2015**, *5* (7), 1401629.
(54) Chatterjee, S.; Shaik, A. K.; Wijesinghe, K. H.; Ndaleh, D.; Dass, A.; Hammer, N. I.; Delcamp, J. H. Design and Synthesis of RhodIndolizine Dyes with Improved Stability and Shortwave Infrared Emission up to 1250 Nm. *J. Org. Chem.* **2022**, *87* (17), 11319−11328.
(55) Wallace, A. M.; Curiac, C.; Delcamp, J. H.; Fortenberry, R. C. Accurate Determination of the Onset Wavelength (Λonset) in Optical Spectroscopy. *J. Quant. Spectrosc. Radiat. Transfer* **2021**, *265*, 107544.
(56) McNamara, L. E.; Rill, T. A.; Huckaba, A. J.; Ganeshraj, V.; Gayton, J.; Nelson, R. A.; Sharpe, E. A.; Dass, A.; Hammer, N. I.; Delcamp, J. H. Indolizine-Squaraines: NIR Fluorescent Materials with Molecularly Engineered Stokes Shifts. *Chem. - Eur. J.* **2017**, *23* (51), 12494−12501.
(57) Dorris, A. L.; Watson, J.; Mosely, J. J.; Lambert, E. C.; Tschumper, G. S.; Delcamp, J. H.; Hammer, N. I. Effects of Proaromaticity on Excited-State Lifetimes and Charge Separation in Near-Infrared Sensitizer Dyes in Solution and on TiO2. *J. Phys. Chem. C* **2023**, *127* (1), 649−659.
(58) Frisch, M. J.; Pople, J. A.; Binkley, J. S. Self-consistent Molecular Orbital Methods 25. Supplementary Functions for Gaussian Basis Sets. *J. Chem. Phys.* **1984**, *80* (7), 3265−3269.
(59) Lee, C.; Yang, W.; Parr, R. G. Development of the Colle-Salvetti Correlation-Energy Formula into a Functional of the Electron Density. *Phys. Rev. B* **1988**, *37* (2), 785−789.
(60) Becke, A. D. Density-functional Thermochemistry. III. The Role of Exact Exchange. *J. Chem. Phys.* **1993**, *98* (7), 5648−5652.
(61) Miertuš, S.; Scrocco, E.; Tomasi, J. Electrostatic Interaction of a Solute with a Continuum. A Direct Utilizaion of AB Initio Molecular Potentials for the Prevision of Solvent Effects. *Chem. Phys.* **1981**, *55* (1), 117−129.
(62) Miertuš, S.; Tomasi, J. Approximate Evaluations of the Electrostatic Free Energy and Internal Energy Changes in Solution Processes. *Chem. Phys.* **1982**, *65* (2), 239−245.
(63) Pascual-ahuir, J. L.; Silla, E.; Tuñon, I. GEPOL: An improved description of molecular surfaces. III. A new algorithm for the computation of a solvent-excluding surface. *J. Comput. Chem.* **1994**, *15* (10), 1127−1138.
(64) Tomasi, J.; Persico, M. Molecular Interactions in Solution: An Overview of Methods Based on Continuous Distribution of the Solvent. *Chem. Rev.* **1994**, *94*, 2027−2094.
(65) Frisch, M. J.; Trucks, G. W.; Schlegel, H. B.; Scuseria, G. E.; Robb, M. A.; Cheeseman, J. R.; Scalmani, G.; Barone, V.; Petersson, G. A.; Nakatsuji, H.; Li, X.; Caricato, M.; Marenich, A. V.; Bloino, J.; Janesko, B. G.; Gomperts, R.; Mennucci, B.; Hratchian, H. P.; Ortiz, J. V.; Izmaylov, A. F.; Sonnenberg, J. L.; Williams-Young, D.; Ding, F.; Lipparini, F.; Egidi, F.; Goings, J.; Peng, B.; Petrone, A.; Henderson, T.; Ranasinghe, D.; Zakrzewski, V. G.; Gao, J.; Rega, N.; Zheng, G.; Liang, W.; Hada, M.; Ehara, M.; Toyota, K.; Fukuda, R.; Hasegawa, J.; Ishida, M.; Nakajima, T.; Honda, Y.; Kitao, O.; Nakai, H.; Vreven, T.; Throssell, K.; Montgomery, J. A., Jr; Peralta, J. E.; Ogliaro, F.; Bearpark, M. J.; Heyd, J. J.; Brothers, E. N.; Kudin, K. N.; Staroverov, V. N.; Keith, T. A.; Kobayashi, R.; Normand, J.; Raghavachari, K.; Rendell, A. P.; Burant, J. C.; Iyengar, S. S.; Tomasi, J.; Cossi, M.; Millam, J. M.; Klene, M.; Adamo, C.; Cammi, R.; Ochterski, J. W.; Martin, R. L.; Morokuma, K.; Farkas, O.; Foresman, J. B.; Fox, D. J. *Gaussian 16, Revision C.01*; Gaussian, Inc.: Wallingford, CT, 2016.
(66) Schleyer, P. v. R.; Maerker, C.; Dransfeld, A.; Jiao, H.; van Eikema Hommes, N. J. R. Nucleus-Independent Chemical Shifts: A Simple and Efficient Aromaticity Probe. *J. Am. Chem. Soc.* **1996**, *118* (26), 6317−6318.
(67) Ditchfield, R. Self-Consistent Perturbation Theory of Diamagnetism. *Mol. Phys.* **1974**, *27* (4), 789−807.
(68) Helgaker, T.; Jaszuński, M.; Ruud, K. Ab Initio Methods for the Calculation of NMR Shielding and Indirect Spin-Spin Coupling Constants. *Chem. Rev.* **1999**, *99* (1), 293−352.
(69) London, F. Théorie quantique des courants interatomiques dans les combinaisons aromatiques. *J. Phys. Radium* **1937**, *8* (10), 397−409.
(70) Wolinski, K.; Hinton, J. F.; Pulay, P. Efficient Implementation of the Gauge-Independent Atomic Orbital Method for NMR Chemical Shift Calculations. *J. Am. Chem. Soc.* **1990**, *112* (23), 8251−8260.
(71) Brogdon, P.; Giordano, F.; Puneky, G. A.; Dass, A.; Zakeeruddin, S. M.; Nazeeruddin, M. K.; Grätzel, M.; Tschumper, G. S.; Delcamp, J. H. A Computational and Experimental Study of Thieno[3,4-b]Thiophene as a Proaromatic π-Bridge in Dye-Sensitized Solar Cells. *Chem. - Eur. J.* **2016**, *22* (2), 694−703.
(72) Yan, J.; Slanina, T.; Bergman, J.; Ottosson, H. Photochemistry Driven by Excited-State Aromaticity Gain or Antiaromaticity Relief. *Chem. - Eur. J.* **2023**, *29* (19), No. e202203748.

https://doi.org/10.1021/acs.joc.4c00741
J. Org. Chem. 2024, 89, 9092−9097